Elucidating failure mechanisms in human femurs during a fall to the side using bilateral digital image correlation

Grassi, Lorenzo; Kok, Joeri; Gustafsson, Anna; Zheng, Yi; Väänänen, Sami P.; Jurvelin, Jukka S.; Isaksson, Hanna

Published in:
Journal of Biomechanics

DOI:
10.1016/j.jbiomech.2020.109826

2020

Document Version:
Publisher's PDF, also known as Version of record

Journal of Biomechanics 106 (2020) 109826

Contents lists available at ScienceDirect

Journal of Biomechanics

journal homepage: www.elsevier.com/locate/jbiomech
www.JBiomech.com

Elucidating failure mechanisms in human femurs during a fall to the side using bilateral digital image correlation

Lorenzo Grassi [a,*], Joeri Kok [a], Anna Gustafsson [a], Yi Zheng [b], Sami P. Väänänen [c,d], Jukka S. Jurvelin [c], Hanna Isaksson [a]

[a] Department of Biomedical Engineering, Lund University, Sweden
[b] Department of Physics, Technical University of Denmark, Denmark
[c] Department of Applied Physics, University of Eastern Finland, Finland
[d] Department of Radiology, Diagnostic Imaging Center, Kuopio University Hospital, Finland

ARTICLE INFO

Article history:
Accepted 5 May 2020

Keywords:
Digital image correlation
Femurs
Sideways fall
Strain distribution
Direction of principal strain
Hip fractures
Mechanical testing

ABSTRACT

An improved understanding of the mechanical properties of human femurs is a milestone towards a more accurate assessment of fracture risk. Digital image correlation (DIC) has recently been adopted to provide full-field strain measurements during mechanical testing of femurs. However, it has typically been used to measure strains on the anterior side of the femur, whereas in both single-leg-stance and sideways fall loading conditions, the highest deformations result on the medial and lateral sides of the femoral neck. The goal of this study was to measure full-field deformations simultaneously on the medial and lateral side of the femoral neck in a configuration resembling a fall to the side. Twelve female cadaver femurs were prepared for DIC measurements and tested in sideways fall at 5 mm/s displacement rate. Two pairs of cameras recorded the medial and lateral side of the femoral neck, and deformations were calculated using DIC. The samples exhibited a two-stage failure: first, a compressive collapse on the superolateral side of the femoral neck in conjunction with peak force, followed by complete femoral neck fracture at the force drop following the post-elastic phase. DIC measurements corroborated this observation by reporting no tensile strains above yield limit for the medial side of the neck up to peak force. DIC measurements registered onto the bone micro-architecture showed strain localizations in proximity of cortical pores due to, for instance, blood vessels. This could explain previously reported discrepancies between simulations and experiments in regions rich with large pores, like the superolateral femoral neck.

1. Introduction

Hip fractures represent a major socioeconomic issue, which is predicted to continue to grow as a consequence of the ageing society (Ahlborg et al., 2010; Svedbom et al., 2013). These fractures are most common in the elderly population (Arakaki et al., 2011) and often result from a relatively low-energy impact such as a fall from standing height (Berry and Miller, 2008; Geusens et al., 2003; Harvey et al., 2016). The current diagnostics based on areal bone mineral density has shown limited accuracy in timely identifying the subjects at risk. About 50% of the women and 70% of the men with a fragility fracture had no osteoporosis at the time of fracture (Sandhu et al., 2010). This has led the biomechanics community to investigate what the true mechanical determinants of femoral strength are. One important part of this investigation consists in using experimental techniques to capture the local mechanical behavior of bone under loading (Cristofolini et al., 2010; Dall'Ara et al., 2013; Fleps et al., 2018; Gilchrist et al., 2013; Rezaei and Dragomir-Daescu, 2015).

For many years, the state-of-the-art method to measure deformations on the surface of femurs during mechanical testing has been to use strain gauges (SGs) (Cristofolini et al., 2010; Grassi and Isaksson, 2015). Despite providing accurate and reliable measurements, SGs are limited to measurement of deformations on a small number of pre-defined regions (maximum 10–15 on a proximal femur (Grassi and Isaksson, 2015)), which is a limitation when investigating the mechanical response in the region where fractures will happen. Digital image correlation (DIC) has been introduced to record the full-field displacements over larger areas of the sample at high spatial resolution (Sutton et al., 1983). DIC is

* Corresponding author at: Department of Biomedical Engineering, Lund University, Box 118, 221 00 Lund, Sweden.
E-mail address: lorenzo.grassi@bme.lth.se (L. Grassi).

https://doi.org/10.1016/j.jbiomech.2020.109826
0021-9290/

a non-contact optical technique that tracks the displacement of randomly distributed speckles during mechanical testing using camera recordings. Deformations can then be derived from the full-field displacements. For samples with high surface curvature, or when out-of-plane motions occur, stereoscopic camera recordings (3D-DIC) are needed (Sutton et al., 2008). While a number of studies used DIC on femurs (Dickinson et al., 2011; Helgason et al., 2014; Jetté et al., 2018; Op Den Buijs and Dragomir-Daescu, 2010; Väänänen et al., 2013), only few have used 3D-DIC on human cadaver femurs (as opposite to composite femurs, which are less clinically relevant (Palanca et al., 2016)). Gilchrist et al. (2013) used 3D-DIC on the anterior surface of the femoral neck, where SG measurements were also simultaneously collected, finding good correlation between the strains measured with the two techniques. The image-to-image noise in DIC was < 6% of the yield strain in bone. The authors of the present study have previously performed 3D-DIC on 3 cadaver femurs (Grassi et al., 2014), collecting deformations on the anterior surface of the femurs during mechanical tests in single-leg-stance configuration. Both these studies used DIC to retrieve the full-field strain pattern on the anterior surface of the femurs. This is likely because the anterior surface is relatively flat and easier to prepare for DIC measurements. However, bone failure is expected to happen either on the medial or lateral side of the femoral neck for the two configurations typically explored during experimental measurements, that is, single-leg-stance and fall to the side (de Bakker et al., 2009).

Consequently, the aim of the present study was to obtain insights on the mechanical behavior of human femurs subjected to a fall to the side using simultaneous 3D-DIC measurements on the medial and lateral sides of the femoral neck.

2. Material and methods

2.1. Material

Twelve fresh-frozen cadaver femurs were collected from female donors (median age 71 years, range 22–88 years, table 1) with no pre-existing conditions known to affect bone metabolism. The Finnish National Authority for Medicolegal Affairs approved collection and use of cadaveric tissue (TEO, 5783/04/044/07). The femurs were imaged with a DXA scanner (Lunar iDXA, GE Healthcare) to obtain areal bone mineral density (aBMD) values. Computed tomography (CT) scans were acquired to compare the deformations measured on the femoral surfaces with the underlying microarchitecture, using two CT scanners: a clinical one (Siemens Somatom AS, pixel size 0.4–0.5 mm, slice separation 0.6 mm, tube voltage 120 kV, tube current 210 mAs) and a high-resolution laboratory x-ray tomographic device (Nikon XT H225, isotropic voxel size 52–60 μm, 100 kVp, 200 mAs).

2.2. Methods

Specimen preparation: soft tissue was removed from the cadaver femurs using scalpel and sandpaper. The femurs were then resected 8 cm distally of the minor trochanter and the most distal 5 cm were embedded in epoxy (Technovit® 4071, Kulzer GmbH) according to the anatomical reference system depicted in Fig. 1. Stainless steel spherical caps were applied with epoxy to the femoral head and the greater trochanter in order to prevent local crushing. The spherical caps were aligned to have their plane perpendicular to the loading direction during the experiment.

The femurs were prepared for DIC measurements by applying a matt white background on the medial and superolateral side of the femoral neck, using spray paint (Dupli-color Platinum, Motip-Dupli GmbH). Following drying of the matt white background, a random speckle pattern was applied using an airbrush spray-pump with a permanent marker, resulting in a coverage of ~ 20–40% and a speckle size of 0.002–0.1 mm^2 (Fig. 1).

Experimental setup: the loading jig was developed based on a previously proposed setup (Zani et al., 2015, 2013), which gave good results in terms of avoiding over-constraints and ability to adjust the sample orientation with ease and accuracy (Fig. 1). Briefly, the distal constraint allowed free tilt in the vertical plane, while all other rotations and translations were constrained. The greater trochanter rested over a system of two orthogonal linear bearings, which minimized any non-vertical force component. The load was applied to the femoral head by the actuator of the testing machine (Instron® 8511.20, Instron Corp) at a controlled speed of 5 mm/s until macroscopic failure of the specimen was reached (defined as a drop in the measured force of 70% of the peak force). The actuator of the testing machine was sprayed with lubricant to minimize non-vertical force components. The femurs were tested in a configuration resembling a posterolateral fall, with an internal rotation of 15° and an adduction angle of 10° (Backman, 1957).

DIC recordings and processing: the experiments were recorded using two pairs of cameras, one recording the medial side of the femoral neck and the second recording the superolateral aspect of the femoral neck.

- The pair of cameras recording the medial side of the femoral neck, hereafter "medial cameras", consisted of two Photron Fastcam Mini AX200 (Photron, Inc.) recording at 6400 fps at 1024 × 1024 pixels (resulting in a resolution of about 20 pixel/mm with the adopted camera positioning), pan angle ~ 16°.
- The pair of cameras recording the superolateral side of the femoral neck, hereafter "lateral cameras", consisted of two Photron Fastcam-X 1280 PCI (Photron, Inc.), recording at 500 fps at 1024 × 1280 pixels (resulting in a resolution of about 18 pixel/mm with the adopted camera positioning), pan angle ~ 38°.

Table 1
Donor information for the twelve femurs used in this study.

Specimen ID	Sex [M/F]	Age [yrs.]	Height [cm]	Weight [kg]	Side [L/R]	$aBMD_{neck}$ [g/cm^2]
CAD045	F	70	164	120	R	0.818
CAD046	F	83	160	56	L	0.670
CAD047	F	68	162	62	L	0.989
CAD049	F	85	160	48	L	0.429
CAD050	F	22	174	96	R	1.053
CAD051	F	67	174	98	R	0.643
CAD052	F	68	N/A	N/A	L	0.739
CAD053	F	88	N/A	N/A	L	0.550
CAD054	F	81	160	67	R	0.736
CAD055	F	80	153	77	L	0.830
CAD057	F	71	166	64	R	0.917
CAD060	F	59	163	55	L	0.971

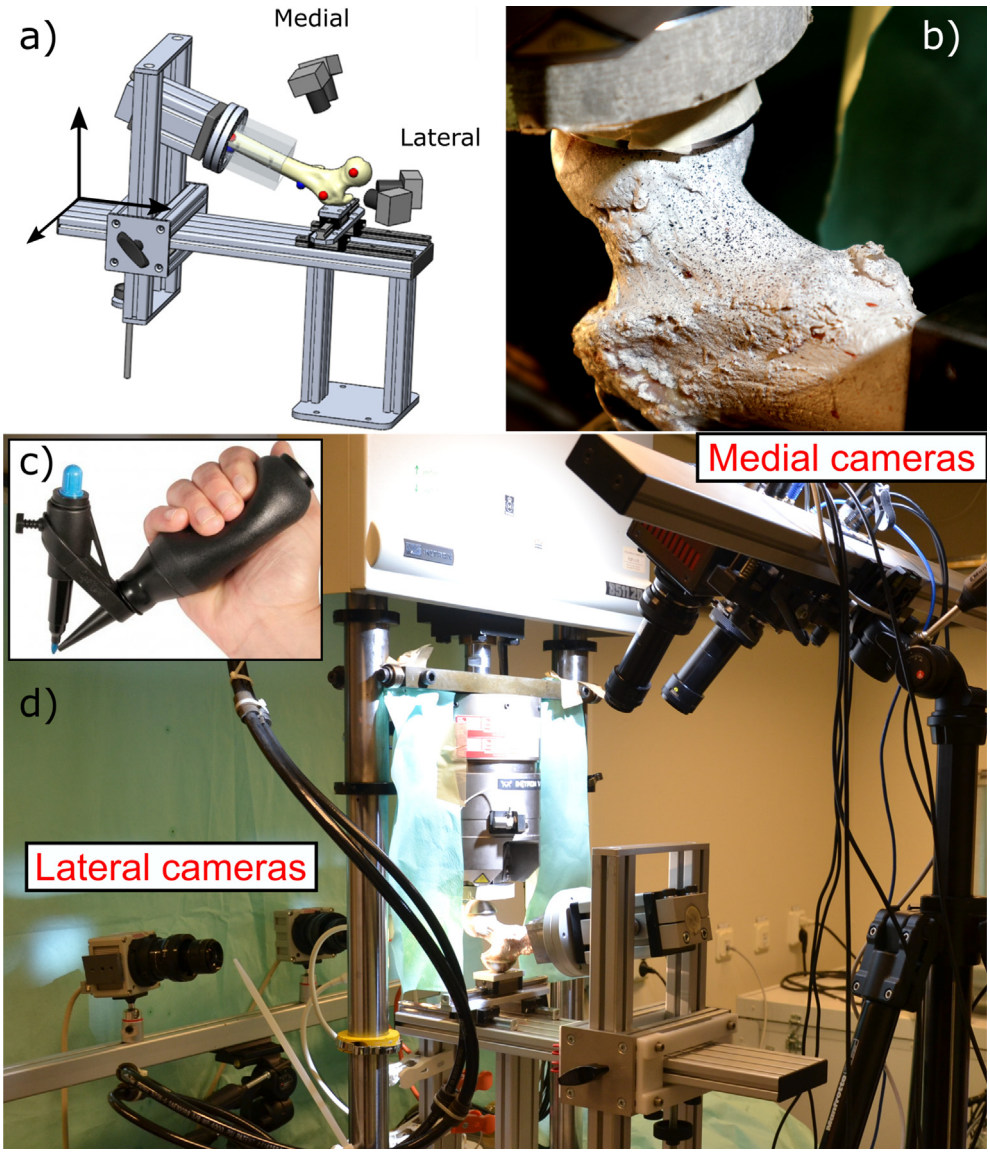

Fig. 1. a) CAD drawing of the jig used to test the femurs in a configuration resembling a fall to the side. The red landmarks define the anatomical frontal plane and were defined as the three contact points of the proximal femur when placed anterior side down on a flat surface. The two blue landmarks define the shaft axis of the femur. The shaft axis together with the anterior plane define the anatomical reference system used to align the samples into the jig. b) Picture of one of the samples placed under the loading jig, the black speckle pattern applied over the medial side of the femoral neck is visible. c) Illustration of the tool used to apply the black speckle pattern. d) A picture of the experimental setup, showing the position of lateral and medial cameras with respect to the tested femur. (For interpretation of the references to color in this figure legend, the reader is referred to the web version of this article.)

The two sets of cameras were simultaneously recording independently of each other, but shared the same end trigger signal, which allowed for synchronization of the recorded images to within one frame of the slowest pair of cameras (corresponding to 2 ms). A digital acquisition system was used (Isi-DAQ-STD-8D, Isi-Sys GmbH) to sample the analogue recordings of the applied force (load cell M211-112, SensorData Technologies, Inc.) and provide measurements of force that were synchronized with the clock signal of the medial cameras. This allowed synchronizing the force–displacement signals recorded at the crosshead of the testing machine with both the medial and lateral camera recordings.

Image correlation was performed with Vic-3D (v7, Correlated Solutions, Inc.). The subset size was chosen as the one that provided an estimated 1-standard deviation confidence in the match below 0.02 pixels, according to the manufacturer's recommendation (Sutton et al., 2009). This resulted in a subset size of 45 pixels for the medial cameras and 35 pixels for the lateral cameras. The step size was 9 pixels for the medial cameras and 5 pixels for the lateral cameras.

The DIC displacements at each point in space were filtered using a low-pass filter in time at a cut-off frequency of 100 Hz. This methodology proved to be effective in removing high-frequency vibration components from the signal whilst being more conservative than conventional filters based on spline fitting of the derived strains (Grassi et al., 2014). Green-Lagrange strain components were derived from the filtered displacement data using a spatial decay filter of 5 data points. These settings resulted in a virtual strain gauge size (that is, the size of the region of the image that affects the strain value at each location, (International Digital Image Correlation Society et al., 2018)) of ~ 4 mm and ~ 3 mm for medial and lateral cameras, respectively.

Data post-processing: from the force–displacement data, peak force was calculated as well as the force at macroscopic failure. The latter was identified as an abrupt change (Killick et al., 2012) in the

mean of the inverse 1-D Haar transform of the applied force signal. Work-to-fracture was calculated for each specimen as the area under the force versus displacement curve until peak force was reached.

The clinical CT images were segmented according to an established procedure (Grassi et al., 2016), whilst the high-resolution CT images were segmented using single threshold. Both geometries were registered to each other and to the DIC data using iterative closest point in CloudCompare (version 2.10.2, www.cloudcompare.org) to allow plotting the DIC measurement over the microstructural features of the bone.

3. Results

Global measurements: The peak force for the twelve samples was 3948 ± 1231 N (range 1515–5477 N, table 2). Macroscopic failure of the samples was reached in 2.04 ± 0.58 s (range 0.72–2.80 s). All force–displacement curves were characterized by a peak force reached within 0.95 ± 0.35 s (range 0.46–1.61 s), followed by a post-elastic phase prior to macroscopic failure of the specimens (Fig. 2). The coefficient of determination R^2 for the displacement–time curves was > 0.99 for all tests. All samples except one exhibited a two-stage fracture. First, there was a collapse in the posterolateral aspect of the femoral neck near the trochanteric fossa, followed by the macroscopic fracture occurring on the medial side of the femoral neck. Please see online supplementary videos V1-V12 to view the synchronized videos of the two camera sets and the force–displacement curves for all femurs. The fractures were classified as 5 pertrochanteric, 5 basicervical, 1 intertrochanteric, 1 midcervical (Table 2 and supplementary Figure A2, ((Meinberg et al., 2018)).

The peak force correlated well with femoral neck aBMD (R^2 = 0.67, RMSE = 739 N, Fig. 3). Linear regression for the peak force as a function of the donors' age indicated a slightly higher correlation when the youngest donor was removed (R^2 = 0.45, RMSE = 925 N) as compared to when all femurs were included (R^2 = 0.42, RMSE = 981 N). This was accompanied by a considerable difference in the slope of the linear regression (−46 N/year versus −87 N/year, Fig. 3). Conversely, the linear regression of the work-to-fracture as a function of age showed a better linear regression where all femurs were included (slope = −289 Nmm/year, R^2 = 0.68, RMSE = 3626 N), compared to when the youngest donor was removed (slope = −300 Nmm/year, R^2 = 0.37, RMSE = 3820 N).

DIC strain data: The strains calculated with DIC from both lateral (major principal strain) and medial (minor principal strain) cameras at four different stages of the test, 50%, 75%, 100% of the peak force and at complete fracture were reported in Fig. 4. The plots showed no tensile strains above the yield limit (7300 με, (Bayraktar et al., 2004)) at peak force, whereas high compressive strains were already present on the superolateral side of the femoral neck. The major principal strain directions on the medial side of the neck aligned more consistently with the neck axis for increased values of the applied force (variance of the polar angle of the major principal strain direction vector going from 133° at 50% of the peak force to 35° at peak force and 8° right before tensile failure, Fig. 5). Conversely, the minor principal strain directions on the superolateral side of the femoral neck were always consistently aligned with the neck axis at the analyzed stages of the load curve (variance of the polar angle of the minor principal strain direction vector always ~ 2°, Fig. 5).

Superimposition of DIC principal strains recorded at 50% of the peak force with the femoral geometry as obtained from segmentation of the high-resolution CT images showed that strain localizations could be detected in proximity of pores in the cortex (caused by, for example, blood vessel insertions, Fig. 6).

Table 2
Peak force, work-to-fracture and fracture classification for the twelve femurs used in this study. The fracture classification was performed by the first author by visual inspection of the samples, based on (Meinberg et al., 2018).

Specimen ID	Peak force [N]	Work-to-fracture [Nmm]	Fracture classification
CADO45	3975	8358	Pertrochanteric
CADO46	2383	3728	Pertrochanteric
CADO47	4451	8876	Basicervical
CADO49	1515	1705	Pertrochanteric
CADO50	5477	23250	Basicervical
CADO51	4531	8895	Intertrochanteric
CADO52	4246	12642	Basicervical
CADO53	4706	12938	Basicervical
CADO54	2520	3443	Pertrochanteric
CADO55	3523	6259	Basicervical
CADO57	4718	7437	Midcervical
CADO60	5325	16901	Pertrochanteric

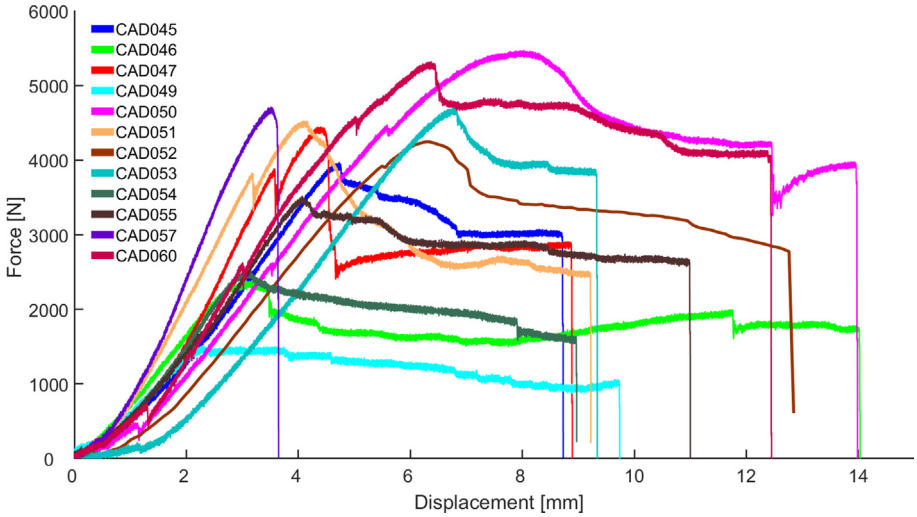

Fig. 2. Force-displacement curves for the twelve samples tested.

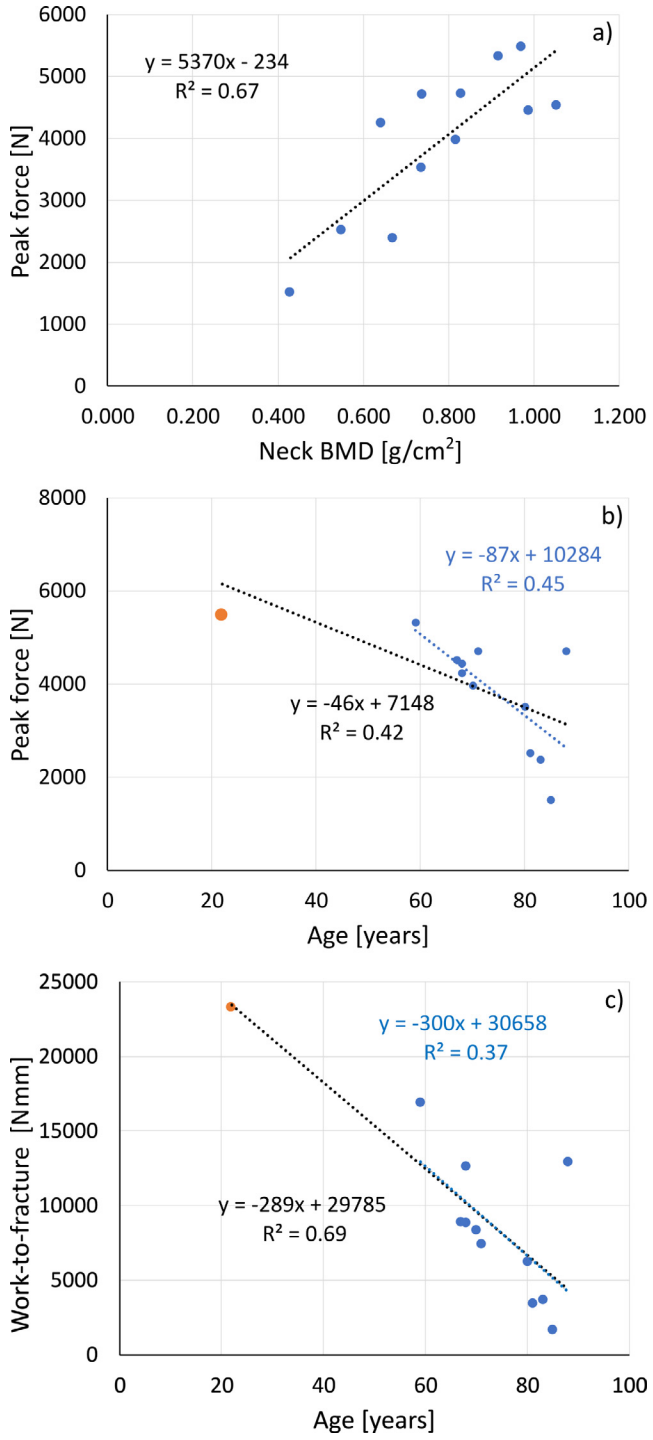

Fig. 3. a) Linear regression for the recorded peak force as a function of femoral neck BMD; b) Linear regression for the recorded peak force as a function of the age of donors at death. Trendlines are shown for all samples together (black) and when CAD050 (depicted in orange) was left out (blue) due to its younger age; c) Linear regression for the work-to-fracture as a function of the age of donors at death. Trendlines are shown for all samples together (black) and when CAD050 (depicted in orange) was left out (blue) due to its younger age.

4. Discussion

The aim of this study was to investigate the local mechanical behavior of human femurs under a loading resembling a fall to the side using simultaneous DIC recordings on the medial and lateral side of the femoral neck.

All 12 femurs but one showed a clear two-stage fracture, as indicated by the force versus displacement curves (Fig. 2). Peak force was followed by a post-elastic phase that lasted until macroscopic failure of the sample; the latter was identified as a crack opening on the medial side of the femur. The simultaneous camera recordings on lateral and medial side of the femoral neck showed that the drop in the reaction force after reaching peak force was associated with compressive damage on the medial side of the femurs (Figs. 4, 5, and supplementary videos V1-V12). These findings were in agreement with previous studies reporting that femoral fractures originate in the superolateral aspect of the femoral neck during sideways fall (de Bakker et al., 2009; Zani et al., 2015). A recent study (Tang et al., 2017) shows that this fracture mechanism is clinically relevant, as compression-induced failure was found in clinical hip fracture cases.

The DIC measurements provided in this study further corroborate the hypothesis of a compressive-induced failure in sideways fall. The strain maps for the two contralateral sides of the femoral neck at different load stages show that the medial aspect of the femoral neck was not subjected to deformations (major principal strains, Fig. 3) above or near the yield limit in tension for cortical bone (7300 με, (Bayraktar et al., 2004)) until peak force had been passed. Conversely, DIC measurements on the lateral side of the femoral neck showed large regions subjected to compressive deformations (minor principal strains, Fig. 4) above the yield limit in compression for trabecular bone (10400 με, (Bayraktar et al., 2004)) already before reaching peak force.

The obtained fractures were classified as 5 pertrochanteric, 5 basicervical, 1 intertrochanteric, 1 midcervical. This distribution of fracture types was in agreement with previous studies using similar setups. Zani et al. (2015) reported 4 intertrochanteric, 4 collapses of greater trochanter, 1 sub-capital and 2 neck fractures using a very similar setup. The updated setup presented in this study managed to avoid the undesired collapses on the greater trochanter. De Bakker et al. (2009) reported 7 neck fractures and 5 intertrochanteric fractures. Interestingly, Fleps et al. (2019) also reported a similar distribution of fracture types (11 bones, 3 non-fractures, 3 intertrochanteric, 1 basicervical, 1 subcapital, 3 pelvic) using a more complex and biofidelic setup that included pelvis compound and soft tissue mimicking in a drop test.

aBMD at the femoral neck was a good predictor of peak force (R^2 = 0.67, RMSE = 739 N, Fig. 3), consistently with previous literature findings (Rezaei and Dragomir-Daescu, 2015). Both peak forces and work-to-fracture correlated well with the age of the donors (Fig. 3). One cadaver was much younger than the rest (age 22, table 1), and by excluding that one from the analysis, the peak force decreased linearly with increasing age: peak force [N] = -87*age [years] + 10284 [N]. This result is in close agreement with what was reported by Rezaei and Dragomir-Daescu (2015) on 67 cadaver femurs from elderly female donors (peak force [N] = −86*age [years] + 9400 [N]). We also calculated the variation of the work-to-fracture as a function of the age and, interestingly, found a good correlation also when including the youngest sample in our cohort (Fig. 3). The authors are not aware of any study reporting work-to-fracture versus age for human femurs, although this is a common metric in animal studies (Carriero et al., 2014; Uppuganti et al., 2016). It is important to point out that the work-to-fracture has been calculated using displacement measurements at the crosshead of the testing machine, thus including the compliance of the experimental setup. This can affect the absolute values of the calculated work-to-fracture. However, the consistency of the boundary conditions and the similar load range between samples (Table 2) suggest that compliance has the same effect on all samples, thus allowing relative comparison. It is therefore interesting to observe how this parameter seems to decline already from a younger age in our sample. Future studies may col-

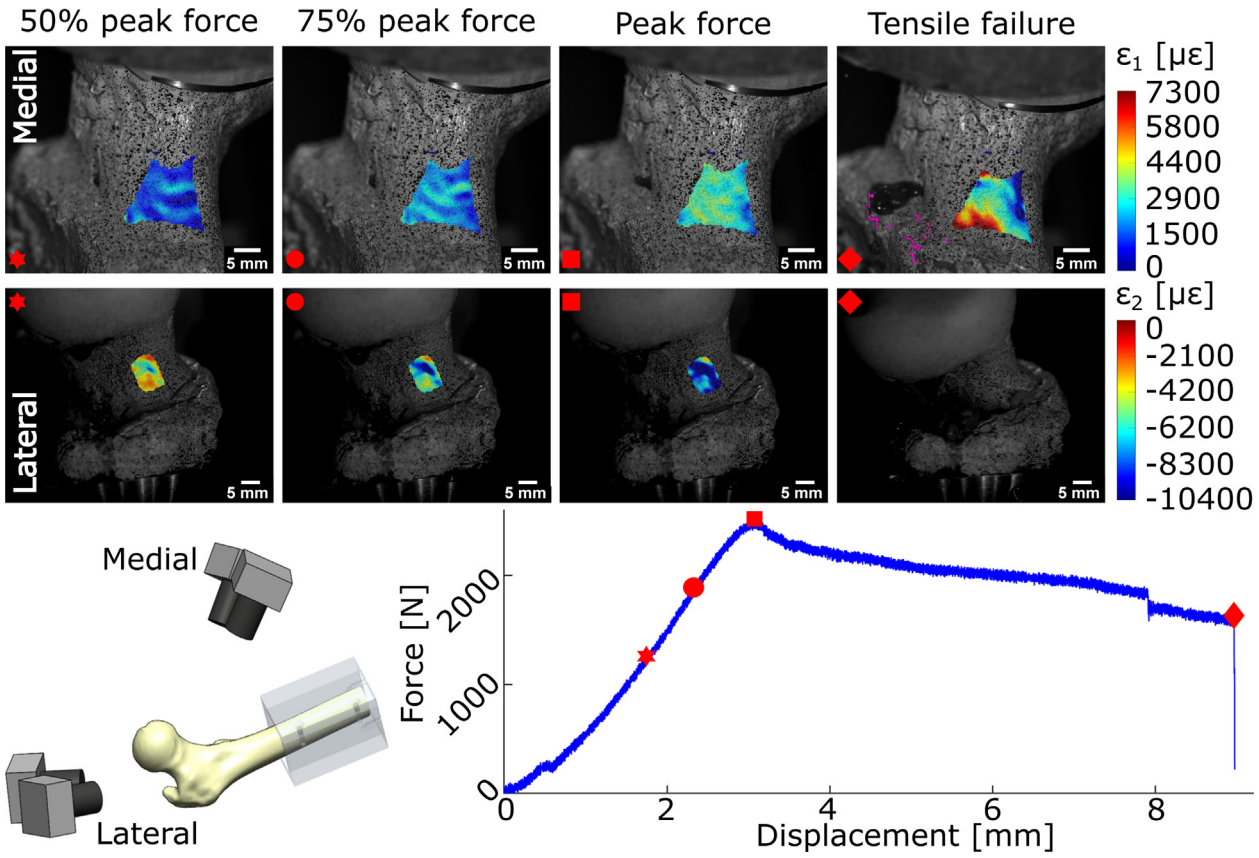

Fig. 4. Major principal strain magnitudes on the medial side of the femoral neck and minor principal strain magnitudes on the superolateral side of the femoral neck for CAD054 at four different stages of the mechanical test: at 50% of the peak force (depicted with an hexagon on the force versus displacement curve), at 75% of the peak force (circle), at peak force (square) and at tensile failure (diamond).

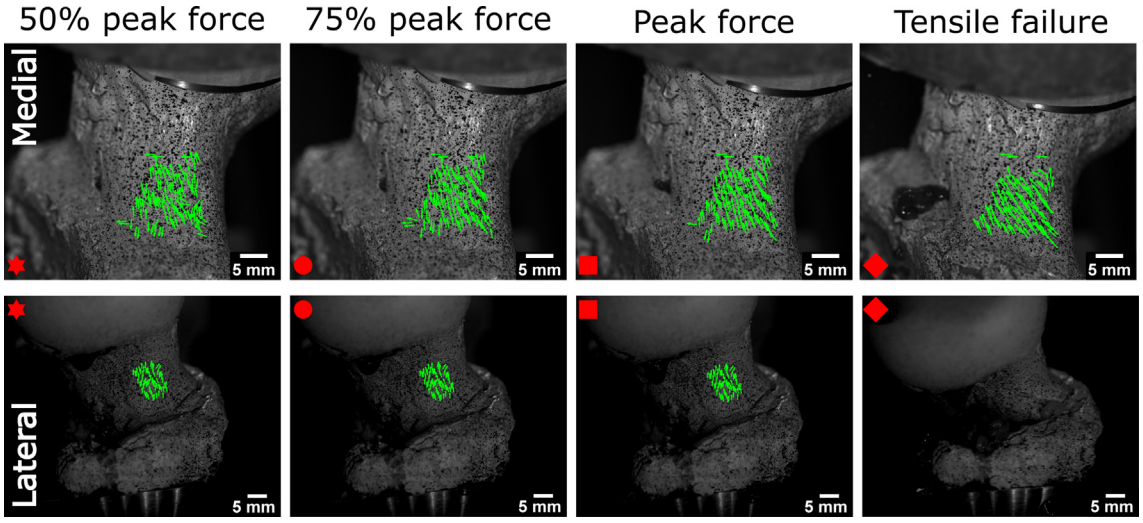

Fig. 5. Major principal strain directions on the medial side of the femoral neck and minor principal strain directions on the superolateral side of the femoral neck for CAD054 at four different stages of the mechanical test: at 50% of the peak force (depicted with an hexagon on the force versus displacement curve), at 75% of the peak force (circle), at peak force (square) and at tensile failure (diamond).

lect data from larger sample cohorts and further investigate such trend, as deeper insights were out of the scopes of the present work.

The present study is the first one reporting a synchronized measurement of strains on the medial and lateral side of the femoral neck during a fall to the side using 3D-DIC. The novelty of this approach came together with some limitations.

One limitation was that the medial cameras had lower recording speed (500 fps versus 6400 fps) than the lateral cameras. The slowest cameras dictated therefore the displacement rate of the

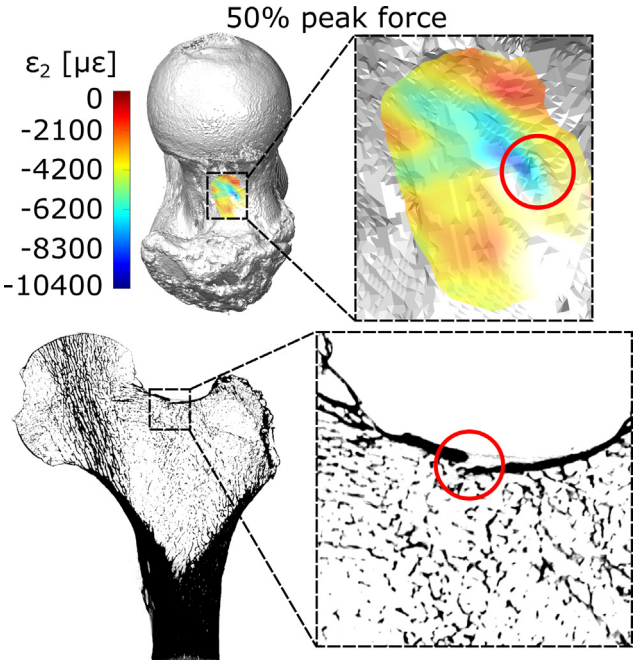

Fig. 6. Minor principal strain magnitudes on the superolateral side of the femoral neck for a force corresponding to 50% of the peak force for CAD054 and superimposed to its micro-architecture as obtained from segmentation of μCT images. A localisation of high compressive strains (circled in red) can be observed in correspondence of a blood vessel on the superolateral side of the femoral neck. In the bottom part of the figure, the same blood vessel insertion is evidenced on a sagittal slide of the high-resolution CT scan.

experiment, which was set to 5 mm/s. This displacement rate is slower than the impact speed of 3 m/s usually reported for falls to the side (Feldman and Robinovitch, 2007; Fleps et al., 2018). However, Gilchrist et al. (2014) reported no differences in terms of energy, yield force and stiffness between impact loading and quasi-static testing conducted in a sideways fall configuration.

A second limitation was that the DIC measurements did not cover the fracture region. Despite recording a broad portion of the medial and lateral sides of the femoral neck with the video cameras, the calculation of DIC had to be limited to a smaller portion of the field of view. This was expected, due to the high curvature of the recorded region and the limited depth of focus. Besides, the compressive collapses in the lateral part of the femoral neck all took place in the trochanteric fossa, which was difficult to record due to the shadowing from the greater trochanter.

Finally, the adopted loading condition (10° adduction, 15° internal rotation) might not be fully representative of a true fall to the side. The same loading configuration has been used by large number of authors in the past (for example, (Courtney et al., 1994; de Bakker et al., 2009; Zani et al., 2015)), but eventually dates back to a study from 1957 (Backman, 1957) where no real physiological explanation was provided for that loading configuration. Nevertheless, the fractures obtained using this loading configuration and the presented setup are in good agreement with findings from clinical fractures (Tang et al., 2017). The presented setup did not include surrogate soft tissue or whole pelvic compounds as in, for example, Fleps et al. (2018). However, such setups are not compatible with full-field strain measurements using optical techniques, which was our focus.

An interesting finding was observed when evaluating together the DIC strain measurements and the micro-architecture of the lateral side of the femoral neck. A localized region experiencing high compressive deformations was detected already at 50% of the peak force on the superolateral side of the femoral neck (Fig. 4). The registration of DIC recordings with the femur geometry obtained from high-resolution CT (Fig. 6) showed that the onset of high compressive strains coincided with the presence of a big pore in the cortex due to a blood vessel insertion. However, compressive failure occurred in the trochanteric fossa, far from the compressive strain localizations. It can be argued that the high compressive strains recorded at low force magnitudes were artefacts due to the movement of the paint covering the blood vessel hole, but it is also possible that the pore triggered a high strain localization. Although we were not able to further corroborate either speculation, this opens interesting questions for the scientific community, as the lateral side of the femoral neck is rich in blood vessel insertions. The fact that their presence has largely been neglected in both experimental measurements and numerical modelling from clinical CT images could explain some of the discrepancies reported in previous literature (Grassi et al., 2012).

In summary, the results presented in this study confirmed previous evidence that femoral fractures during a sideways fall are the result of a compressive failure of the femoral neck. The synchronized camera recordings and the associated DIC measurements on both medial and lateral side of the femoral neck corroborated this finding. The DIC measurements could also be used in future studies as a comprehensive benchmark for subject-specific finite element models, allowing full-field strain validation on the more relevant regions for proximal femur fractures.

Acknowledgement

We thank Lilly Dawson and Sara Panzetta for contributing to develop the experimental setup; Jonas Engqvist and Stephen Hall for lending out Vic-3D license; Christoffer Johansson for lending out one camera pair. The study received funding from Swedish Research Council (2015-4795), Swedish Foundation for Strategic Research (IB2013-0021), and Birgit and Hellmuth Hertz' Foundation.

Conflict of interest statement

The authors declare that there is no conflict of interest regarding the publication of this article.

Appendix A. Supplementary data

Supplementary data to this article can be found online at https://doi.org/10.1016/j.jbiomech.2020.109826.

References

Ahlborg, H.G., Rosengren, B.E., Järvinen, T.L.N., Rogmark, C., Nilsson, J.-A., Sernbo, I., Karlsson, M.K., 2010. Prevalence of osteoporosis and incidence of hip fracture in women–secular trends over 30 years. BMC Musculoskelet. Disord. 11, 48. https://doi.org/10.1186/1471-2474-11-48.

Arakaki, H., Owan, I., Kudoh, H., Horizono, H., Arakaki, K., Ikema, Y., Shinjo, H., Hayashi, K., Kanaya, F., 2011. Epidemiology of hip fractures in Okinawa. Japan. J. Bone Miner. Metab. 29, 309–314. https://doi.org/10.1007/s00774-010-0218-8.

Backman, S., 1957. The proximal end of the femur: investigations with special reference to the etiology of femoral neck fractures; anatomical studies; roentgen projections; theoretical stress calculations; experimental production of fractures. Acta Radiol. Suppl., 1–166

Bayraktar, H.H., Morgan, E.F., Niebur, G.L., Morris, G.E., Wong, E.K., Keaveny, T.M., 2004. Comparison of the elastic and yield properties of human femoral trabecular and cortical bone tissue. J. Biomech. 37, 27–35. https://doi.org/10.1016/S0021-9290(03)00257-4.

Berry, S.D., Miller, R.R., 2008. Falls: epidemiology, pathophysiology, and relationship to fracture. Curr. Osteoporos. Rep. 6, 149–154.

Carriero, A., Zimmermann, E.A., Shefelbine, S.J., Ritchie, R.O., 2014. A methodology for the investigation of toughness and crack propagation in mouse bone. J. Mech. Behav. Biomed. Mater. 39, 38–47. https://doi.org/10.1016/j.jmbbm.2014.06.017.

Courtney, A.C., Wachtel, E.F., Myers, E.R., Hayes, W.C., 1994. Effects of loading rate on strength of the proximal femur. Calcif. Tissue Int. 55, 53–58.
Cristofolini, L., Conti, G., Juszczyk, M., Cremonini, S., Van Sint Jan, S., Viceconti, M., 2010. Structural behaviour and strain distribution of the long bones of the human lower limbs. J. Biomech. 43, 826–835. https://doi.org/10.1016/j.jbiomech.2009.11.022.
Dall'Ara, E., Luisier, B., Schmidt, R., Kainberger, F., Zysset, P., Pahr, D., 2013. A nonlinear QCT-based finite element model validation study for the human femur tested in two configurations in vitro. Bone 52, 27–38. https://doi.org/10.1016/j.bone.2012.09.006.
de Bakker, P.M., Manske, S.L., Ebacher, V., Oxland, T.R., Cripton, P.A., Guy, P., 2009. During sideways falls proximal femur fractures initiate in the superolateral cortex: evidence from high-speed video of simulated fractures. J. Biomech. 42, 1917–1925. https://doi.org/10.1016/j.jbiomech.2009.05.001.
Dickinson, A.S., Taylor, A.C., Ozturk, H., M, B., 2011. Experimental validation of a finite element model of the proximal femur using digital image correlation and a composite bone model. J. Biomech. Eng. 133, 014504. https://doi.org/10.1115/1.4003129.
Feldman, F., Robinovitch, S.N., 2007. Reducing hip fracture risk during sideways falls: evidence in young adults of the protective effects of impact to the hands and stepping. J. Biomech. 40, 2612–2618. https://doi.org/10.1016/j.jbiomech.2007.01.019.
Fleps, I., Guy, P., Ferguson, S.J., Cripton, P.A., Helgason, B., 2019. Explicit Finite Element Models Accurately Predict Subject-Specific and Velocity-Dependent Kinetics of Sideways Fall Impact. J. Bone Miner. Res. https://doi.org/10.1002/jbmr.3804.
Fleps, I., Vuille, M., Melnyk, A., Ferguson, S.J., Guy, P., Helgason, B., Cripton, P.A., 2018. A novel sideways fall simulator to study hip fractures ex vivo. PLoS ONE 13,. https://doi.org/10.1371/journal.pone.0201096 e0201096.
Geusens, P., Milisen, K., Dejaeger, E., Boonen, S., 2003. Falls and fractures in postmenopausal women: a review. J. Br. Menopause Soc. 9, 101–106. https://doi.org/10.1258/136218003100322314.
Gilchrist, S., Guy, P., Cripton, P. a, 2013. Development of an inertia-driven model of sideways fall for detailed study of femur fracture mechanics. J. Biomech. Eng. 135, 121001. https://doi.org/10.1115/1.4025390.
Gilchrist, S., Nishiyama, K.K., de Bakker, P., Guy, P., Boyd, S.K., Oxland, T., Cripton, P. A., 2014. Proximal femur elastic behaviour is the same in impact and constant displacement rate fall simulation. J. Biomech. 47, 3744–3749. https://doi.org/10.1016/j.jbiomech.2014.06.040.
Grassi, L., Isaksson, H., 2015. Extracting accurate strain measurements in bone mechanics A critical review of current methods. J. Mech. Behav. Biomed. Mater. 50, 43–54. https://doi.org/10.1016/j.jmbbm.2015.06.006.
Grassi, L., Schileo, E., Taddei, F., Zani, L., Juszczyk, M., Cristofolini, L., Viceconti, M., 2012. Accuracy of finite element predictions in sideways load configurations for the proximal human femur. J. Biomech. 45, 394–399. https://doi.org/10.1016/j.jbiomech.2011.10.019.
Grassi, L., Väänänen, S.P., Amin Yavari, S., Jurvelin, J.S., Weinans, H., Ristinmaa, M., Zadpoor, A.A., Isaksson, H., 2014. Full-Field Strain Measurement During Mechanical Testing of the Human Femur at Physiologically Relevant Strain Rates. J. Biomech. Eng. 136,. https://doi.org/10.1115/1.4028415 111010.
Grassi, L., Väänänen, S.P., Ristinmaa, M., Jurvelin, J.S., Isaksson, H., 2016. How accurately can subject-specific finite element models predict strains and strength of human femora? Investigation using full-field measurements. J. Biomech. 49, 802–806. https://doi.org/10.1016/j.jbiomech.2016.02.032.
Harvey, N., Odén, A., Orwoll, E., Lapidus, J., Kwok, T., Karlsson, M., Rosengren, B., Ljunggren, O., Cooper, C., McCloskey, E., Kanis, J., Ohlsson, C., Mellström, D., Johansson, H., 2016. Falls Predict Fractures Independently of FRAX Probability: The Osteoporotic Fractures in Men (MrOS) Study Author(s). Abstr. ASBMR Annu. Meet. 1078. https://doi.org/10.1002/jbmr.3331.
Helgason, B., S Gilchrist, Ariza, O., Chak, J.D., Zheng, G., Widmer, R.P., Ferguson, S.J., Guy, P., Cripton, P. a, 2014. Development of a balanced experimental-computational approach to understanding the mechanics of proximal femur fractures. Med. Eng. Phys. 36, 793–799. https://doi.org/10.1016/j.medengphy.2014.02.019.
International Digital Image Correlation Society, Jones, E., Iadicola, M., Bigger, R., Blaysat, B., Boo, C., Grewer, M., Hu, J., Jones, A., Klein, M., Raghavan, K., Reu, P., Schmidt, T., Siebert, T., Simenson, M., Turner, D., Vieira, A., Weikert, T., 2018. A Good Practices Guide for Digital Image Correlation. International Digital Image Correlation Society. https://doi.org/10.32720/idics/gpg.ed1.
Jetté, B., Brailovski, V., Simoneau, C., Dumas, M., Terriault, P., 2018. Development and in vitro validation of a simplified numerical model for the design of a biomimetic femoral stem. J. Mech. Behav. Biomed. Mater. 77, 539–550. https://doi.org/10.1016/j.jmbbm.2017.10.019.
Killick, R., Fearnhead, P., Eckley, I.A., 2012. Optimal Detection of Changepoints With a Linear Computational Cost. J. Am. Stat. Assoc. 107, 1590–1598. https://doi.org/10.1080/01621459.2012.737745.
Meinberg, E.G., Agel, J., Roberts, C.S., et al., 2018. Fracture and Dislocation Classification Compendium - 2018. J Orthop Trauma. 32 (Supplement 1), S1–S170.
Op Den Buijs, J., Dragomir-Daescu, D., 2010. Validated finite element models of the proximal femur using two-dimensional projected geometry and bone density. Comput. Methods Programs Biomed. 104, 1–7. https://doi.org/10.1016/j.cmpb.2010.11.008.
Palanca, M., Tozzi, G., Cristofolini, L., 2016. The use of digital image correlation in the biomechanical area: a review. Int. Biomech. 3, 1–21. https://doi.org/10.1080/23335432.2015.1117395.
Rezaei, A., Dragomir-Daescu, D., 2015. Femoral Strength Changes Faster with Age than BMD in Both Women and Men: A Biomechanical Study. J. Bone Miner. Res. n/a-n/a. https://doi.org/10.1002/jbmr.2572.
Sandhu, S.K., Nguyen, N.D., Center, J.R., Pocock, N.A., Eisman, J.A., Nguyen, T.V., 2010. Prognosis of fracture: Evaluation of predictive accuracy of the FRAX™ algorithm and Garvan nomogram. Osteoporos. Int. 21, 863–871. https://doi.org/10.1007/s00198-009-1026-7.
Sutton, M., Wolters, W., Peters, W., Ranson, W., McNeill, S., 1983. Determination of displacements using an improved digital correlation method. Image Vis. Comput. 1, 133–139. https://doi.org/10.1016/0262-8856(83)90064-1.
Sutton, M.A., Orteu, J.J., Schreier, H., 2009. Image Correlation for Shape, Motion and Deformation Measurements: Basic Concepts, Theory and Applications, Theory ApplSpringer. Springer. https://doi.org/10.1007/978-0-387-78747-3_1.
Sutton, M.A., Yan, J.H., Tiwari, V., Schreier, H.W., Orteu, J.-J., 2008. The effect of out-of-plane motion on 2D and 3D digital image correlation measurements. Opt. Lasers Eng. 46, 746–757. https://doi.org/10.1016/j.optlaseng.2008.05.005.
Svedbom, A., Hernlund, E., Ivergård, M., Compston, J., Cooper, C., Stenmark, J., McCloskey, E.V., Jönsson, B., Kanis, J.A., 2013. Osteoporosis in the European Union: A compendium of country-specific reports. Arch. Osteoporos. 8. https://doi.org/10.1007/s11657-013-0137-0.
Tang, T., Cripton, P.A., Guy, P., McKay, H.A., Wang, R., 2017. Clinical hip fracture is accompanied by compression induced failure in the superior cortex of the femoral neck. Bone 108, 121–131. https://doi.org/10.1016/j.bone.2017.12.020.
Uppuganti, S., Granke, M., Makowski, A.J., Does, M.D., Nyman, J.S., 2016. Age-related Changes in the Fracture Resistance of Male Fischer F344 Rat Bone. Bone 83, 220–232. https://doi.org/10.1016/j.bone.2015.11.009.
Väänänen, S.P., Amin Yavari, S., Weinans, H., Zadpoor, A.A., Jurvelin, J.S., Isaksson, H., 2013. Repeatability of digital image correlation for measurement of surface strains in composite long bones. J. Biomech. 46, 1928–1932. https://doi.org/10.1016/j.jbiomech.2013.05.021.
Zani, L., Cristofolini, L., Juszczyk, M.M., Grassi, L., Viceconti, M., 2013. A new paradigm for the in vitro simulation of sideways fall loading of the proximal human femur. J. Mech. Med. Biol. 14, 1450005. https://doi.org/10.1142/S0219519414500055.
Zani, L., Erani, P., Grassi, L., Taddei, F., Cristofolini, L., 2015. Strain distribution in the proximal Human femur during in vitro simulated sideways fall. J. Biomech. 48, 2130–2143. https://doi.org/10.1016/j.jbiomech.2015.02.022.